Supplementary Information

Optical Trapping Theory of Graphene

To calculate the radiation force[1] and torque[2] we use the full scattering theory in the transition matrix (T-matrix) approach[3]. This is quite general as it applies to particles of any shape and refractive index, and for wavelength. The starting point is the calculation of the field configuration in the focal region of a high NA objective lens in absence of any particle[4]. The resulting field is considered as the field incident on the particles, and the radiation force and torque exerted on any particle within the region is calculated using linear and angular momentum conservation for the combined system of field and particles[5]. We adopt the geometry sketched in Fig.S1. The coordinate systems $Oxyz$ is linked to the laboratory and $O'x'y'z'$ to the local frame of reference with origin in the center of mass of the flake. The z' and y' axes are parallel to the long and short edge of the rectangular model flake. The incident wave is a x-polarized gaussian beam focalized through a NA=1.3 objective (as in our experiments).

In the graphene frame of reference, the optical force and torque are[1, 6]:

$$\mathbf{F}_{\mathrm{Rad}} = \quad r'^2 \int_{\Omega'} \hat{\mathbf{r}}' \cdot \langle \mathbf{T}_{\mathrm{M}} \rangle d\Omega', \tag{1}$$

$$\mathbf{G}_{\mathrm{Rad}} = -r'^3 \int_{\Omega'} \hat{\mathbf{r}}' \cdot \langle \mathbf{T}_{\mathrm{M}} \rangle \times \hat{\mathbf{r}} d\Omega', \tag{2}$$

where the integration is on the full solid angle, r' is the radius of a large sphere surrounding graphene, $\langle \mathbf{T}_{\mathrm{M}} \rangle$ is the time averaged Maxwell stress tensor:

$$\langle \mathbf{T}_{\mathrm{M}} \rangle = \frac{1}{8\pi} \mathrm{Re} \left[n^2 \mathbf{E}' \otimes \mathbf{E}'^* + \mathbf{B}' \otimes \mathbf{B}'^* - \frac{1}{2}(n^2 |\mathbf{E}'|^2 + |\mathbf{B}'|^2) \mathbf{I} \right], \tag{3}$$

where $\otimes$ denotes dyadic product, $\mathbf{I}$ is the unit dyadic and n is the refractive index of water. The fields that enter Eq.3 are the superposition of incident and scattered. Thus $\mathbf{E}' = \mathbf{E}'_{\mathrm{I}} + \mathbf{E}'_{\mathrm{S}}$ and $\mathbf{B}' = \mathbf{B}'_{\mathrm{I}} + \mathbf{B}'_{\mathrm{S}}$. When the incident field is a polarized plane wave, the radiation force components along a direction defined by a unit vector $\hat{\mathbf{v}}_\zeta$ are[1]:

$$F_{\mathrm{Rad}\,\zeta} = -\frac{r'^2}{16\pi} \mathrm{Re} \int_{\Omega'} (\hat{\mathbf{r}}' \cdot \hat{\mathbf{v}}_\zeta) [n^2 (|\mathbf{E}'_{\mathrm{S}}|^2 + 2\mathbf{E}'^*_{\mathrm{I}} \cdot \mathbf{E}'_{\mathrm{S}}) + (|\mathbf{B}'_{\mathrm{S}}|^2 + 2\mathbf{B}'^*_{\mathrm{I}} \cdot \mathbf{B}'_{\mathrm{S}})] \, \mathrm{d}\Omega' \, . \tag{4}$$

In turn the radiation torque takes the form:

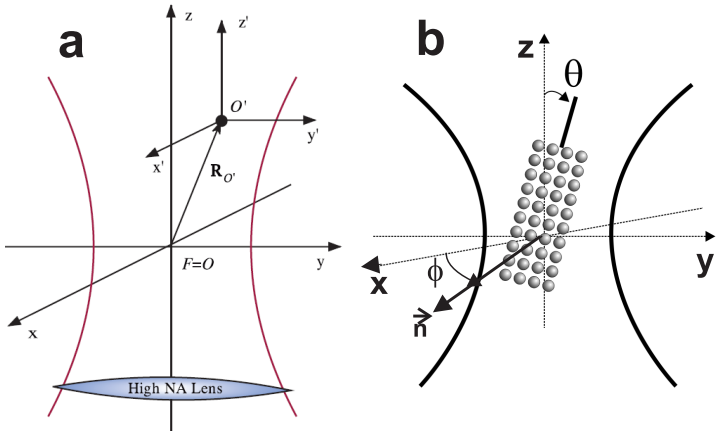

Figure S1: (a) Local frame of reference attached to the model graphene. (b) Flake geometry with respect to the optical trap coordinate system.

$$\mathbf{G}_{\mathrm{Rad}} = -\frac{r'^3}{8\pi}\mathrm{Re}\int_{\Omega'}[n^2(\hat{\mathbf{r}}'\cdot\mathbf{E}')\mathbf{E}'^{*}\times\hat{\mathbf{r}}' + (\hat{\mathbf{r}}'\cdot\mathbf{B}')\mathbf{B}'^{*}\times\hat{\mathbf{r}}']\mathrm{d}\Omega' \ , \tag{5}$$

where $\mathbf{E}' = \mathbf{E}'_{\mathrm{I}} + \mathbf{E}'_{\mathrm{S}}$ and $\mathbf{B}' = \mathbf{B}'_{\mathrm{I}} + \mathbf{B}'_{\mathrm{S}}$. We expand both $\mathbf{E}'_{\mathrm{I}}$ and $\mathbf{E}'_{\mathrm{S}}$ in a series of vector spherical multipole fields in the form:

$$\mathbf{E}'_{\mathrm{I}} = \quad E_0 \textstyle\sum_{plm} \mathbf{J}^{(p)}_{lm}(\mathbf{r}', k) W^{(p)}_{lm}(\hat{\mathbf{e}}_{\mathrm{I}}, \hat{\mathbf{k}}_{\mathrm{I}}) \tag{6}$$

$$\mathbf{E}'_{\mathrm{S}} = \quad E_0 \textstyle\sum_{plm} \mathbf{H}^{(p)}_{lm}(\mathbf{r}', k) A^{(p)}_{lm}(\hat{\mathbf{e}}_{\mathrm{I}}, \hat{\mathbf{k}}_{\mathrm{I}}) \ , \tag{7}$$

whence the multipole expansions of $\mathbf{B}'_{\mathrm{I}}$, $\mathbf{B}'_{\mathrm{S}}$ are obtained from $\mathbf{B}' = -\frac{i}{k}\nabla\times\mathbf{E}'$. In Eq. 6 $\mathbf{J}^{(p)}_{lm}$ denote multipole fields everywhere regular, and the amplitudes $W^{(p)}_{lm}$ are known. In Eq. 7 $\mathbf{H}^{(p)}_{lm}$ denote multipole fields that satisfy the radiation condition at infinity and the amplitudes $A^{(p)}_{lm}$ have arguments $\hat{\mathbf{e}}_{\mathrm{I}}$ and $\hat{\mathbf{k}}_{\mathrm{I}}$, to recall that they depend on the polarization and direction of propagation of the incident field, with:

$$A^{(p)}_{lm} = \sum_{p'l'm'} \mathcal{S}^{(pp')}_{lml'm'} W^{(p')}_{l'm'} \tag{8}$$

the elements of the graphene transition matrix. These are calculated in a given frame of reference through the inversion of the matrix of the linear system obtained by imposing to the fields boundary conditions across the

graphene surface. Note that the T-matrix elements are independent both on propagation and polarization of the incident field. Thus they do not change when the incident field is a superposition of plane waves with the same propagation constant, but different direction of propagation, as for a focused laser beam in the angular spectrum representation[3, 7].

We model graphene as a planar aggregate of small (3nm) subunit spheres. Their size and number are chosen to have a transverse size comparable with the experimental flakes. The light scattering properties of this planar aggregate are regulated by the subunit size parameter[3], $x = 2\pi nr/\lambda$, with $n = 1.33$ refractive index of the surrounding medium, r radius of the subunit sphere, and $\lambda = 830$nm trapping wavelength in vacuo. Since the subunit size parameter is small, $x \approx 0.03 \ll 1$, the light scattering (and optical trapping) properties of the graphene flake are well approximated by our model[8].

The dielectric constant of graphene is a highly anisotropic tensor[9]. When the incident polarization lies in the graphene plane, i.e. orthogonal to the flake main axis, the dielectric constant is $\varepsilon_\perp$. Whereas for polarization orthogonal to the graphene plane, i.e. parallel to its main axis $\vec{n}$ (see Fig. S4), the dielectric constant is $\varepsilon_\parallel$. At the wavelength of our optical trapping experiments ($\lambda = 830\,\mathrm{nm}$), $n_\perp = 3 + i\,1.5$ and $n_\parallel = 1.694$[9].

Stable trapping is achieved when the graphene plane is parallel to yz, and the long axis is aligned with the optical (z-)axis of the system, as shown in Fig.4 of the main text. Note that when the polarization axis lies on the graphene plane (e.g. when parallel to xy or xz), the radiation pressure is so strong that graphene is pushed out of the trap. This is a consequence of the large imaginary part of $\varepsilon_\perp$. As shown in Fig.4 of the main text, graphene is stable under small angle rotations around its equilibrium orientation, while for larger values of ϕ and θ it is expelled by radiation pressure.

Graphene Hydrodynamics

The dynamics of graphene in dispersion encompasses translational and rotational motions. For such anisotropic particles, the viscous drag and torque are described by anisotropic friction tensors[10, 11] γ^t_{ij}, for translations, and γ^r_{ij}, for rotations. These are related to the fluid (water) dynamical viscosity η and particle sizes along its main axis. From HRTEM, our flakes can be well described as extremely flat ellipsoids with transverse size Δ much larger than their height h. We can then exploit the set of analytic solutions for uniaxial ellipsoids obtained by Perrin[12]. For an oblate ellipsoid with semiaxes

$a < b, c$ the elliptic integral parameter is[12]:

$$S = \frac{2}{\sqrt{b^2 - a^2}} \arctan \frac{\sqrt{b^2 - a^2}}{a} \tag{9}$$

The friction coefficients[11] of the diagonal matrices, referred to the ellipsoid main axes, are[12]:

$$\gamma_a^t = \gamma_\parallel = 16\pi\eta \frac{a^2 - b^2}{(2a^2 - b^2)S - 2a} \tag{10}$$

$$\gamma_b^t = \gamma_c^t = \gamma_\perp = 32\pi\eta \frac{a^2 - b^2}{(2a^2 - 3b^2)S + 2a} \tag{11}$$

$$\gamma_a^r = \frac{32}{3}\pi\eta \frac{(a^2 - b^2)b^2}{2a - b^2 S} \tag{12}$$

$$\gamma_b^r = \gamma_c^r = \frac{32}{3}\pi\eta \frac{a^4 - b^4}{(2a^2 - b^2)S - 2a} \tag{13}$$

For SLG, $a \ll b = c \approx \Delta/2$ and the elliptic integral parameter only depends on flake diameter:

$$S \approx \pi/b \approx 2\pi/\Delta \tag{14}$$

Thus in the same approximation the hydrodynamic friction coefficients are expressed only as a function of the water viscosity and flake diameter:

$$\gamma_\parallel = 8\eta\Delta; \quad \gamma_\perp = \frac{16}{3}\eta\Delta; \quad \gamma^r = \frac{4}{3}\eta\Delta^3 \tag{15}$$

In this approximation the rotational friction has the same value for any axis passing through the graphene center-of-mass, while the translation coefficients parallel and perpendicular to the symmetry axis have a 3/2 ratio.

Our flakes have $\Delta \approx 25$nm, $\eta = 0.91$mPa s so that $\gamma_\parallel \sim 0.182$(fN s)/$\mu$m, $\gamma_\perp \sim 0.121$ (fN s)/μm and $\gamma^r \sim 1.9 \times 10^{-2}$fNnms. Thus the mobility coefficients, $\Gamma_{ij} = \gamma_{ij}^{-1}$, are $\Gamma_\parallel \sim 5.49$ μm/(fN s), $\Gamma_\perp \sim 8.26$ μm/(fN s) and $\Gamma^r \sim 52.6$ (fN nm s)$^{-1}$. The uncertainty on these values is linked to that of the flake size. Since the size distribution has a $\sim$40% spread, we expect an uncertainty on the hydrodynamic parameters of the same order.

Langevin equations

In order to understand the Langevin dynamics of trapped graphene, we approximate the optical tweezers as an harmonic potential $V(x_i) = \frac{1}{2}\sum_{i=x,y,z} k_i x_i^2$

with spring constants k_x, k_y, k_z[1, 13]. The rigid motion is described through the Euler angles ϕ, θ, ψ[14]. We consider graphene as an oblate ellipsoid, so that $\psi = 0$ due to rotational symmetry. Thus, the corresponding rotation matrix from the laboratory coordinates x_i to the internal coordinates (aligned with the principal inertia axes of the ellipsoid) $x'_i = \mathcal{R}_{ij}(\phi, \theta)\, x_i$ is[14]:

$$\mathcal{R}(\phi,\theta) = \begin{pmatrix} \cos\phi & \sin\phi & 0 \\ -\cos\theta\sin\phi & \cos\theta\cos\phi & \sin\theta \\ \sin\theta\sin\phi & -\sin\theta\cos\phi & \cos\theta \end{pmatrix} \tag{16}$$

Furthermore we are interested only in the small angles ($\phi, \theta \ll 1$) fluctuations around equilibrium in the yz-plane (the plane orthogonal to the polarization axis $\vec{n}$, see Fig.S1b). Thus the rotation matrix simplifies to:

$$\mathcal{R}(\phi,\theta) \approx \begin{pmatrix} 1 & \phi & 0 \\ -\phi & 1 & \theta \\ 0 & -\theta & 1 \end{pmatrix} \tag{17}$$

The torque exerted by the optical harmonic potential is the sum of the center of mass and inner torques. The center of mass coordinates, X_i, are uncorrelated stochastic variables. Thus, the time average of crossed terms of the type $X_i X_j$ can be neglected, so that they do not give a contribution to the Brownian dynamics[15, 13]. Hence, the only relevant contributions to the angular fluctuations are the inner torque components $M_i(\phi, \theta)$. These are calculated by integrating over the ellipsoid mass density distribution $\rho(x'_i)$[13]:

$$\begin{aligned} M_i(\phi,\theta) &= -\int d^3x' \frac{\rho(x'_i)}{m} \epsilon_{ijl} x_j k_l x_l \\ &= -\int d^3x' \frac{\rho(x'_i)}{m} \epsilon_{ijl} \left[\mathcal{R}^{-1}(\phi,\theta)\vec{x}'\right]_j k_l \left[\mathcal{R}^{-1}(\phi,\theta)\vec{x}'\right]_l \end{aligned} \tag{18}$$

where k_i are the spring constants of the trapping potential, ϵ_{ijl} is the Levi-Civita symbol[14], and m is the mass of the trapped object. Thus, we can write the torque components using the moments of inertia of the oblate ellipsoid $I_\perp = \int d^3x' \rho(x'_i)\,[x'^2 + z'^2]$ and $I_\parallel = \int d^3x' \rho(x'_i)\,[y'^2 + z'^2]$ (referred to rotation perpendicular and parallel to x′, the ellipsoid symmetry axis):

$$M_x \approx 0 \tag{19}$$

$$M_y \approx -(k_x - k_z)\frac{I_\parallel - I_\perp}{m}\theta = -k_\theta \theta \tag{20}$$

$$M_z \approx -(k_y - k_x)\frac{I_\parallel - I_\perp}{m}\phi = -k_\phi \phi \tag{21}$$

Note that $M_x \approx 0$ because we assumed rotational symmetry around x'. A breaking of this symmetry yields a contribution to the x-component of the torque that will tend to align the flake with its longer axis parallel to z (see Fig.4 of the main text). Thus, for small angles, the torque exerted by the harmonic potential is independent by translations and the dynamics of the flake is described by a set of five uncoupled stochastic variables X, Y, Z, ϕ, θ.

In order to calculate the Langevin equations[15] in the lab frame, we recall that the friction force and torque exerted by the fluid on the fluctuating particle (Stokes force and torque) are expressed in term of the hydrodynamic mobilities (obtained as the inverse of Eq.15) so that:

$$\begin{aligned} \partial_t X(t) &= -\Gamma_{\parallel} k_x X(t) + \xi_x(t) \\ \partial_t Y(t) &= -\Gamma_{\perp} k_y Y(t) + \xi_y(t) \\ \partial_t Z(t) &= -\Gamma_{\perp} k_z Z(t) + \xi_z(t) \\ \partial_t \phi(t) &= -\Gamma^r k_\phi \phi(t) + \xi_\phi(t) \\ \partial_t \theta(t) &= -\Gamma^r k_\theta \theta(t) + \xi_\theta(t) \end{aligned} \tag{22}$$

where $\xi_i(t)$ are random noise sources with zero mean and variance $\langle \xi_i(t)\xi_i(t+\tau)\rangle = 2k_BT\Gamma_i\delta(\tau)$ (with $\delta(\tau)$ Dirac's δ). These lead to first order differential equations for the corresponding autocorrelation functions $C_{X_iX_i}(\tau) = \langle X_i(t)X_i(t+\tau)\rangle$ and $C_{\phi\phi}(\tau) = \langle \phi(t)\phi(t+\tau)\rangle$, $C_{\theta\theta}(\tau) = \langle \theta(t)\theta(t+\tau)\rangle$, e.g. for $X(t)$ the corresponding autocorrelation function is:

$$\partial_\tau C_{XX}(\tau) = -\Gamma_{\parallel} k_x C_{XX}(\tau) \tag{23}$$

that yields an exponential decay:

$$C_{XX}(\tau) = \frac{k_BT}{k_x} e^{-\Gamma_{\parallel} k_x |\tau|} \tag{24}$$

Thus, the corresponding autocorrelation functions for the five stochastic variables X, Y, Z, ϕ, θ decay with relaxation frequencies:

$$\begin{aligned} \omega_x = \Gamma_{\parallel} k_x,\ \omega_y = \Gamma_{\perp} k_y,\ \omega_z = \Gamma_{\perp} k_z \\ \Omega_\phi = \Gamma^r k_\phi,\ \Omega_\theta = \Gamma^r k_\theta. \end{aligned} \tag{25}$$

Note that we only considered the torque exerted by an *uncoupled* potential on a rigid body. Real graphene flakes have anisotropic polarizability that introduces additional contributions to the components M_y, M_z of the torque. Thus, the total optical torque on a tilted flake might be expected to have a nonlinear dependence with the angular displacement.

Correlation functions of the signals.

For trapped graphene the interference pattern in the objective BFP can change in two cases: a) the flake is orthogonal to the polarization axis and the interference changes because of center of mass displacements (X,Y,Z). Thus in the linear regime the QPD signals are proportional to these displacements. b) The flake is tilted by a small angle θ or ϕ, so that the change in BFP interference and QPD signals are proportional (to first approximation) to the (oriented) projections of the flake on the lab frame axes. Thus, in the limit of small angles, $\theta \ll 1, \phi \ll 1$, and, under the assumptions discussed above, the QPD signals can be expressed in the lab frame as a superposition of the center of mass displacements and angular tilting:

$$S_x \sim \beta_x \left(X - \mathrm{a}\,\phi + \mathrm{b}\,\theta\right);\; S_y \sim \beta_y \left(Y + \mathrm{c}\,\phi\right);\; S_z \sim \beta_z Z \tag{26}$$

where a,b,c are constants that depend on flake geometry and optical constants. β_i are calibration factors that convert the QPD signals in displacements. They can be obtained from the amplitude of the autocorrelation functions after evaluation of the spring constants by using the equipartition theorem $\beta_i = k_i C_{ii}(0)/k_B T$[16, 13, 17]. From Fig.4 of the main text, we measure $\beta_x \approx 0.07\,V/\mu m$, $\beta_y \approx 0.069\,V/\mu m$, $\beta_z \approx 0.27\,V/\mu m$. These enable the conversion from V to μm for the BM plots shown in the main text.

The center-of-mass X_i and angular ϕ, θ coordinates are stochastic variables. The QPD autocorrelation functions $C_{ii}(\tau) = \langle S_i(t) S_i(t+\tau)\rangle$ are:

$$C_{xx} \approx \beta_x^2 \left[C_{XX} + \mathrm{A}^2\, C_{\phi\phi} + \mathrm{B}^2\, C_{\theta\theta}\right] \tag{27}$$

$$C_{yy} \approx \beta_y^2 \left[C_{YY} + \mathrm{C}^2\, C_{\phi\phi}\right] \tag{28}$$

$$C_{zz} \approx \beta_z^2\, C_{ZZ} \tag{29}$$

where we assume center-of-mass and angular fluctuations to be uncorrelated, thus neglect cross terms of type $\langle X_i(t)\phi(t+\tau)\rangle$, $\langle X_i(t)\theta(t+\tau)\rangle$ and $\langle \phi(t)\theta(t+\tau)\rangle$. Thus, the QPD autocorrelations give combined information on center-of-mass and angular fluctuations, and decay with lag time τ as multiple-exponentials with separated positional and angular relaxation frequencies.

The angular fluctuations yield non-zero cross-correlations of the QPD signals $C_{ij}(\tau) = \langle S_i(t) S_j(t+\tau)\rangle$ $(i \neq j)$:

$$C_{xy} \approx -\beta_x \beta_y \mathrm{AC}\, C_{\phi\phi}; \quad C_{xz} \approx 0; \quad C_{yz} \approx 0 \tag{30}$$

Thus, C_{xy} decays as a single exponential (Eq.22) with relaxation rate corresponding to Ω_ϕ i.e. directly connected to the optical torque constant k_ϕ, and rotational hydrodynamic mobility Γ^r.

Note that we obtained the QPD signals assuming displacements within a linear response and with small cross-talk (that we estimate experimentally to be $\sim$5%). Equations 27-29 fit well our experimental data with two exponential decays. We have a good understanding of the change of sign in the cross-correlation functions occurring because of the planar graphene geometry. Note that from our data the θ fluctuations are at the noise level. We extracted information on k_ϕ and verified that the graphene displacements in the trap are within the linear response.

Frame sequence

Figure S2 is a sequence of frames extracted from the Supplementary Movie. When the laser is on, the flake is trapped in the focal region of the laser beam (Fig.S2A). The flake has dimensions below the wavelength of light used for imaging. The transverse size results from integration of the interference between scattered and unscattered light on the CCD camera, i.e. only a diffraction limited spot can be imaged. When the flake is trapped, its Brownian fluctuations occur on a spatial range smaller than the image resolution, at a rate faster than the acquisition frame rate. Instead, when the laser is off (Figs.S2B-I), the flake is not trapped and changes its dynamical configuration at all time scales. Thus, each image from Fig.S2B-I is a snapshot of the random displacements resulting from the free BM. Finally, in the movie the laser is turned on and the flake is trapped again. The change from dark to bright spot in Figs.S2F,G is due to phase change of the illumination while the flake passes through the image plane of the microscope objective.

References

[1] F. Borghese, P. Denti, R. Saija, M.A. Iatì, Optical trapping of nonspherical particles in the T-matrix formalism. *Opt. Exp.* **15**, 11984 (2007).

[2] F. Borghese et al. Radiation force and torque on optically trapped linear nanostructures. *Phys. Rev. Lett.* **100**, 163903 (2008).

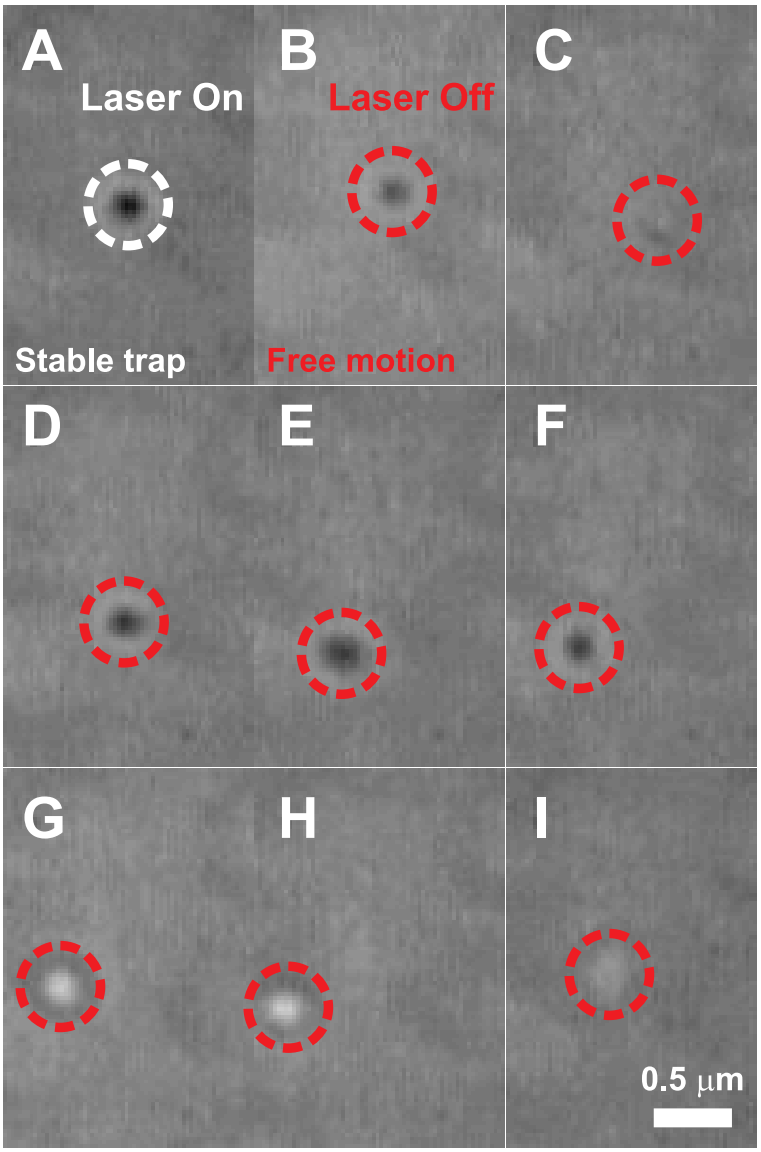

Figure S2: When the laser is on (**a**), the flake is trapped and oriented in the focal region of the beam. When off (**b-i**), the flake is not trapped and fluctuates in both position and orientation. The images on the CCD result from the diffraction and interference of light from the flake.

[3] F. Borghese, P. Denti, R. Saija, *Scattering from model nonspherical particles*, 2nd ed. (Springer,Berlin,2007).

[4] B. Richards, E. Wolf, Electromagnetic Diffraction in Optical Systems. II. Structure of the Image Field in an Aplanatic System. *Proc. R. Soc. London Ser. A*, **253**, 358-379, (1959).

[5] J.D. Jackson, *Classical Electrodynamics*,(Wiley, New York, 1975).

[6] F. Borghese et al., Radiation torque on nonspherical particles in the transition matrix formalism *Opt. Expr.* **14**, 9508-9521 (2006).

[7] L. Novotny, B. Hecht, *Principles of nano-optics*, (CU. Press, 2006).

[8] R. Saija et al. Backscattered Intensity from Model Atmospheric Ice Crystals in the Millimeter-Wave Range. *Appl. Opt.* **40**, 5337-5342 (2001).

[9] V.G. Kravets, *et al.*, Spectroscopic ellipsometry of graphene. *Phys. Rev. B* **81**, 155413 (2010).

[10] J. Happel, H. Brenner, *Low Reynolds Number Hydrodynamics*, Springer, Berlin, (1981).

[11] X. Sun, T. Lin, J.D. Gezelter, Langevin dynamics for rigid bodies of arbitrary shape. *J. Chem. Phys.* **128**, 234107 (2008).

[12] F. Perrin, Mouvement Brownien d'un ellipsoide (I). Dispersion diélectrique pour des molécules ellipsoidales. *J. Phys. Rad* **5**, 497 (1934).

[13] O.M. Maragò, *et al.* Femotonewton force sensing with optically trapped carbon nanotubes. *Nano Lett.* **8**, 3211-3216 (2008).

[14] H. Goldstein, C.P. Poole, J.L. Safko, *Classical Mechanics*, 3rd ed. (Addison Wesley, 2001).

[15] W.T. Coffey, Y.P. Kalmykov, J.T. Waldron, *The Langevin Equation*, 2nd ed. (World Scientific, Singapore, 2004).

[16] A. Pralle, *et al.* Three-Dimensional High-Resolution Particle Tracking for Optical Tweezers. *Micr. Res. Tech.* **44**, 378-386 (1999).

[17] G. Volpe, D. Petrov, Torque detection using brownian fluctuations. *Phys. Rev. Lett.* **97**, 210603 (2006).